JOURNAL OF GUIDANCE, CONTROL, AND DYNAMICS
Vol. 20, No. 2, March–April 1997

Articulated, Flexible Multibody Dynamics Modeling: Geostationary Operational Environmental Satellite-8 Case Study

Sivakumar S. K. Tadikonda*
McDonnell Douglas Aerospace, Seabrook, Maryland 20706

The attitude dynamics of Geostationary Operational Environmental Satellite-8 (GOES-8) is simulated using an articulated, flexible multibody approach, and simulation results are compared with the spacecraft flight data. The solar array on this spacecraft is lightweight and flexible and is actuated by a stepper motor. The stepping harmonics are shown to excite the vibrational modes of the solar array. Angular displacement sensors for each of the spacecraft attitude degrees of freedom provided data accurate to subarcsecond levels. The simulations provided insights into the on-orbit behavior of the solar array as a function of time of day. The solar array modal data required modifications to obtain a good agreement with the flight data. Several causes that could necessitate these modifications are identified. The assumptions behind the structural dynamics modeling and the articulated multibody modeling of the three-dimensional flexible solar array are highlighted. Although the GOES-8 was not set up to provide a platform for validating multibody dynamics models or approaches, it is concluded that these approaches can indeed be employed for simulating the dynamics of other spacecraft or flexible manipulators even when accuracies at the subarcsecond level are involved.

Nomenclature

$\mathbf{b}_i$ = $[\underline{b}_{i1}\ \ \underline{b}_{i2}\ \ \underline{b}_{i3}]^T$, a Cartesian body frame and the associated unit vectors
C_0^s = $\mathbf{b}_s \cdot \mathbf{b}_0^T = (C_s^0)^T$, transformation matrix between $\mathbf{b}_s$ and $\mathbf{b}_0$
$\boldsymbol{h}^{(i)}$ = a $3 \times N_i$ rigid body rotational–elastic motion coupling (modal angular momentum coefficient) matrix for body i, expressed in $\mathbf{b}_i$.
$\boldsymbol{I}_i$ = inertia matrix for body i about the hinge point in its own coordinate system
$\boldsymbol{I}_s$ = inertia matrix for the spacecraft bus about the origin of the body frame, expressed in the bus body frame
i = body index: $i = s$ for the bus, $i = 0$ for inertial frame, $i = 1$ for solar array, and $i = 2$ for solar sail
$\boldsymbol{K}^{(i)}$ = $N_i \times N_i$ modal stiffness matrix for the solar array. (If the modes are mass normalized, this matrix will be diagonal with the squares of the frequencies (in radians) as the elements.)
$\underline{\ell}$ = unit vector along the rotational axis of the solar array; $\ell = \mathbf{b}_s \cdot \underline{\ell}$
m_i = mass of body i
N_i = number of component modes used in modeling body i flexibility
$\boldsymbol{R}$ = $[R_x\ \ R_y\ \ R_z]^T$, components of $\underline{R}$ in $\mathbf{b}_0$; $\boldsymbol{R} = \mathbf{b}_0 \cdot \underline{R}$
$\underline{R}$ = position vector locating the spacecraft body frame with respect to $\mathbf{b}_0$
$\tilde{\boldsymbol{r}}$ = a 3×3 skew symmetric matrix formed using the (three) components of any 3×1 column matrix $\boldsymbol{r}$
$\boldsymbol{r}_c^{(i)}$ = components of vector $\underline{r}_c^{(i)}$ to the center of mass of body i from the hinge point; $\boldsymbol{r}_c^{(i)} = \mathbf{b}_i \cdot \underline{r}_c^{(i)}$
$\boldsymbol{r}_i$ = components of vector $\underline{r}_i$ from the origin of $\mathbf{b}_s$ to the body i-spacecraft interface point; $\boldsymbol{r}_i = \mathbf{b}_s \cdot \underline{r}_i$
$\boldsymbol{V}$ = components of $\dot{\underline{R}}$ expressed in $\mathbf{b}_s$; $\boldsymbol{V} = \mathbf{b}_s \cdot \dot{\underline{R}}$
$\boldsymbol{\alpha}^{(i)}$ = a $3 \times N_i$ rigid body translational–elastic motion coupling (modal linear momentum coefficient) matrix for body i, expressed in $\mathbf{b}_i$
$\eta_1^{(i)}\eta_2^{(i)} \ldots \eta_{N_i}^{(i)}$ = time-dependent modal amplitudes for body i
θ = variable describing articulation of solar array with respect to spacecraft bus
$\boldsymbol{\omega}_s$ = a 3×1 column matrix containing spacecraft angular velocity components in $\mathbf{b}_s$

Introduction

THE Geostationary Operational Environmental Satellite-8 (GOES-8) shown in Fig. 1 belongs to the GOES/I-M weather satellite series; after the launch on April 13, 1994, GOES-I was renamed GOES-8. Each of these spacecraft has a solar sail and a magnetometer boom, both rigidly attached to the spacecraft, and an articulating solar array that is driven by a stepper motor. In the baseline stepping mode of the array, a single step corresponding to a 0.007-deg rotation occurs every 1.69 s. The array and the sail have four- and five-component fixed-free vibrational modes, respectively, with frequencies below 2 Hz. The first fixed–free component natural frequency of the magnetometer boom is over 4.5 Hz. Of these, the first torsional mode of the array is expected to be excited most by the constant stepping of the solar-array drive motor. A solar x-ray imager (SXI) is to be flown on the yoke of the solar array on GOES-M, scheduled for launch in 1999, and the jitter environment for the SXI needed to be quantified. Since all GOES/I-M spacecraft have the same kinematic structure and possess similar mass properties, it was determined that any model that is developed for predicting the SXI jitter must be validated first by comparison with the flight data of one of the predecessors to GOES-M. GOES-8 is instrumented with an angular displacement sensor (ADS) for each axis of the spacecraft to study fine spacecraft motions. The ADS can measure attitude accurately to an arcsecond. One SXI pixel corresponds to 5 arcseconds and thus ADS provides precisely the capability needed for predicting the SXI jitter.

Often, in the space industry, the analysis of unmanned spacecraft with flexible appendages begins with the assumption that the attitude and the vibrational motions of the spacecraft are uncoupled. Such analyses are performed for bounding the spacecraft jitter

Received Jan. 2, 1996; presented as Paper 96-3887 at the AIAA Guidance, Navigation, and Control Conference and Exhibit, San Diego, CA, July 29–31, 1996; revision received Nov. 20, 1996; accepted for publication Nov. 26, 1996.

*Senior Principal Engineer, Engineering Services Division, 7404 Executive Place. Member AIAA.

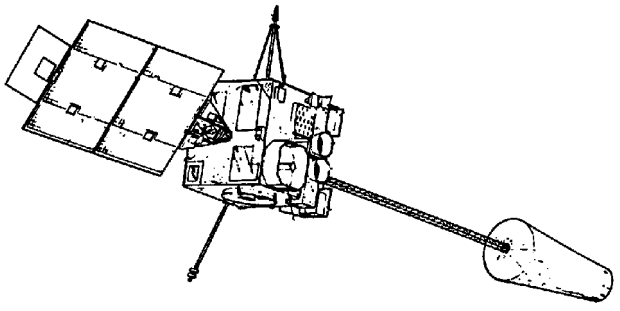

Fig. 1 GOES-8 spacecraft.

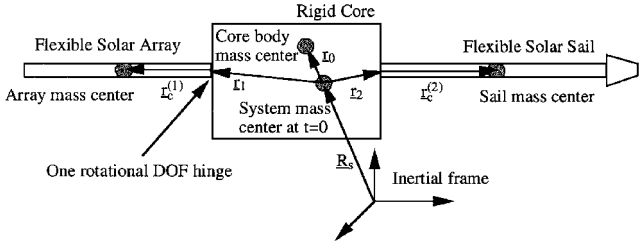

Fig. 2 GOES-8 diagram.

due to instrument disturbances. Recognizing that the validity of this assumption is limited to spacecraft that contain only nonarticulating appendages, analyses of spacecraft with articulating flexible appendages, such as solar arrays, are performed for different but fixed orientations of the appendage. Consequently, in the articulating appendage cases, such analyses omit the transition between those orientations.

This is in contrast to analyzing models based on articulated, flexible multibody approaches,[1–3] or simulating the response using articulated multibody dynamic analysis tools, such as TREETOPS[2] and DISCOS,[3] that correctly model the array articulation. It is shown using flight data that, in the case of GOES-8, the persistent disturbance on the spacecraft is due to the articulation of the solar array, and in particular due to the stepping process. As a result, modeling the transition between different solar-array orientations, even if they are only 0.007 deg (one step for the stepper motor) apart, is paramount for correctly simulating spacecraft response. Consequently, an articulated, flexible multibody dynamics model of GOES-8 is employed in this study.

Component flexible-body models are used for the solar array and the solar sail. The magnetometer boom is modeled as a rigid body and its mass properties are combined with those of the spacecraft bus. Although the dynamic equations can be derived using any of the approaches in Refs. 1–3, this is the first time that spacecraft flight data at the subarcsecond level are compared successfully with simulation results from an articulated, flexible multibody dynamic model, to the best of the author's knowledge. It is not very often that a spacecraft is instrumented with a fine attitude motion sensor such as the ADS to present such an opportunity. The dynamic model, the simulation results, and the lessons learned during the course of this study are presented in this paper. Note that the modeling issues addressed in this paper are not limited to GOES-8 and are applicable to any spacecraft or articulating flexible multibody sytem.

Dynamic Model

A diagram of GOES-8 is shown in Fig. 2. The central body (bus) and the magnetometer boom are modeled as rigid and are treated as one body, and the already available component flexible-body modal models for the solar array and the solar sail are used along with an assumed modes approach.[4] The component flexible-body data are obtained via finite element analyses using NASTRAN. The system now consists of three translational and three attitude degrees of freedom (DOFs) of the bus, one solar-array articulated DOF, and N_1 and N_2 modal DOFs associated with the solar array and the solar sail, respectively. In general, underlined characters represent vectors and boldfaced characters represent matrices of appropriate dimensions. Let

$$\boldsymbol{v} = \left[\boldsymbol{V}^T \boldsymbol{\omega}_s^T \; \dot{\theta} \; \dot{\eta}_1^{(1)} \; \dot{\eta}_2^{(1)} \; \ldots \; \dot{\eta}_{N_1}^{(1)} \; \dot{\eta}_1^{(2)} \; \dot{\eta}_2^{(2)} \; \ldots \; \dot{\eta}_{N_2}^{(2)}\right]^T \tag{1}$$

where the superscript T denotes transpose, the overdot represents differentiation with respect to time, and

$$\boldsymbol{V} = \boldsymbol{C}_0^s \dot{\boldsymbol{R}} \tag{2}$$

The system mass matrix then is given by

$$\boldsymbol{M} = \begin{bmatrix} m_t \boldsymbol{U} & -m_t \tilde{\boldsymbol{r}}_c & [0] & \boldsymbol{C}_1^s \boldsymbol{\alpha}^{(1)} & \boldsymbol{\alpha}^{(2)} \\ & \boldsymbol{I}_{\text{sys}} & \boldsymbol{I}_q \boldsymbol{\ell} & \tilde{\boldsymbol{r}}_1 \boldsymbol{C}_1^s \boldsymbol{\alpha}^{(1)} + \boldsymbol{C}_1^s \boldsymbol{h}^{(1)} & \boldsymbol{h}^{(2)} \\ & & \boldsymbol{\ell}^T \boldsymbol{I}_1 \boldsymbol{\ell} & \boldsymbol{\ell}^T \boldsymbol{h}^{(1)} & [0] \\ & \text{Sym} & & [1] & [0] \\ & & & & [1] \end{bmatrix} \tag{3}$$

where $m_t = m_s + m_1 + m_2$ denotes the total mass, $\boldsymbol{r}_c$ contains the components of the vector to the instantaneous system mass center in $\mathbf{b}_s$, $\boldsymbol{U}$ is a 3×3 identity matrix, and [0] and [1] denote null and identity matrices of appropriate dimensions. The two diagonal blocks of [1] represent $N_1 \times N_1$ and $N_2 \times N_2$ identity matrices and these represent the mass normalized modal mass matrices of the solar array and the solar sail, respectively. When the assumed modes method[4] is used to express the elastic displacement $\underline{u}^{(i)}(\underline{r}, t)$ as

$$\underline{u}^{(i)}(\underline{r}, t) = \sum_{j=1}^{N_i} \underline{\phi}_j^{(i)}(\underline{r}) \eta_j^{(i)}(t) \tag{4}$$

in terms of the assumed-mode shapes $\underline{\phi}_j^{(i)}(\underline{r})$ and their amplitudes $\eta_j^{(i)}(t)$, the modal linear momentum coefficients $\underline{\alpha}_j^{(i)}$ and the modal angular momentum coefficients $\underline{h}_j^{(i)}$ are defined as[5,6]

$$\underline{\alpha}_j^{(i)} = \int_{\text{body } i} \underline{\phi}_j^{(i)}(\underline{r}) \, \mathrm{d}m \tag{5}$$

and

$$\underline{h}_j^{(i)} = \int_{\text{body } i} \underline{r} \times \underline{\phi}_j^{(i)}(\underline{r}) \, \mathrm{d}m \tag{6}$$

The momentum coefficients are computed in the component body frame. In addition,

$$\boldsymbol{\alpha}_j^{(i)} = \mathbf{b}_i \cdot \underline{\alpha}_j^{(i)}; \qquad \boldsymbol{h}_j^{(i)} = \mathbf{b}_i \cdot \underline{h}_j^{(i)} \tag{7}$$

The remaining quantities appearing in Eq. (3) have the following expansions:

$$\begin{aligned} \boldsymbol{I}_{\text{sys}} &= \boldsymbol{I}_s + \boldsymbol{I}_1 + \boldsymbol{I}_2 + m_1 \left(\boldsymbol{r}_1^T \boldsymbol{r}_1 \boldsymbol{U} - \boldsymbol{r}_1 \boldsymbol{r}_1^T\right) \\ &\quad + m_1 \left[2\boldsymbol{r}_1^T \boldsymbol{C}_1^s \boldsymbol{r}_c^{(1)} \boldsymbol{U} - \boldsymbol{r}_1 \left(\boldsymbol{C}_1^s \boldsymbol{r}_c^{(1)}\right)^T - \boldsymbol{C}_1^s \boldsymbol{r}_c^{(1)} \boldsymbol{r}_1^T\right] \\ &\quad + m_2 \left(\boldsymbol{r}_2^T \boldsymbol{r}_2 \boldsymbol{U} - \boldsymbol{r}_2 \boldsymbol{r}_2^T + 2\boldsymbol{r}_2^T \boldsymbol{r}_c^{(2)} \boldsymbol{U} - \boldsymbol{r}_2 \boldsymbol{r}_c^{(2)^T} - \boldsymbol{r}_c^{(2)} \boldsymbol{r}_2^T\right) \end{aligned} \tag{8}$$

$$\boldsymbol{I}_q = \boldsymbol{I}_1 + m_1 \left(\boldsymbol{r}_1^T \boldsymbol{C}_1^s \boldsymbol{r}_c^{(1)} \boldsymbol{U} - \boldsymbol{C}_1^s \boldsymbol{r}_c^{(1)} \boldsymbol{r}_1^T\right) \tag{9}$$

Let $\boldsymbol{K}$ be defined as

$$\boldsymbol{K} = \begin{bmatrix} [0]_{7\times 7} & [0]_{7\times N_1} & [0]_{7\times N_2} \\ [0]_{N_1\times 7} & \boldsymbol{K}^{(1)} & [0]_{N_1\times N_2} \\ [0]_{N_2\times 7} & [0]_{N_2\times N_1} & \boldsymbol{K}^{(2)} \end{bmatrix} \tag{10}$$

Note that the flexibility in the system is associated only with the solar array and the solar sail. This is the reason that the first seven rows and seven columns of the system stiffness matrix $\boldsymbol{K}$ corresponding to rigid body motions contain only zeros. In addition, we define a damping matrix $\boldsymbol{D}$ with the same structure as that of $\boldsymbol{K}$, with diagonal viscous modal damping blocks for the flexible bodies. Let $\boldsymbol{q}$ be defined as a $(7 + N_1 + N_2) \times 1$ column matrix of displacement coordinates such that

$$\boldsymbol{q} = \left[\boldsymbol{R}^T \; \theta_x \; \theta_y \; \theta_z \; \theta \; \eta_1^{(1)} \eta_2^{(1)} \; \ldots \; \eta_{N_1}^{(1)} \; \eta_1^{(2)} \; \eta_2^{(2)} \; \ldots \; \eta_{N_2}^{(2)}\right]^T \tag{11}$$

The first six variables represent the spacecraft position and attitude DOFs. Since $\boldsymbol{V}$ and $\boldsymbol{\omega}_s$ are components in a rotating body frame, they cannot be integrated to obtain the displacements/orientations. Equation (2) must be integrated to obtain the position of the spacecraft, and the following equation must be integrated to obtain the attitude $(\theta_x, \theta_y, \theta_z)$

$$\dot{\boldsymbol{C}}_0^s + \tilde{\boldsymbol{\omega}}_s \boldsymbol{C}_0^s = \boldsymbol{0} \tag{12}$$

The system equations of motion can then be written as

$$\boldsymbol{M}\dot{\boldsymbol{v}} + \boldsymbol{D}\dot{\boldsymbol{q}} + \boldsymbol{K}\boldsymbol{q} + \boldsymbol{G}(\boldsymbol{q}, \boldsymbol{v}) = \mathcal{U} \tag{13}$$

where $\boldsymbol{G}(\boldsymbol{q}, \boldsymbol{v})$ is a column matrix containing nonlinear terms and $\mathcal{U}$ is a column matrix containing excitations/disturbances.

Stepper motor tests indicated that the motor behaves like an underdamped second-order system. Consequently, the stepping action of the motor is modeled using a PD controller:

$$\mathcal{U}(7) = -[\Omega^2(\theta - \hat{\theta}) + 2\zeta\Omega\dot{\theta}]\boldsymbol{I}_1(2, 2) \tag{14}$$

where $\hat{\theta}$ represents the desired angle and is increased by 0.007 deg at the beginning of every step, and Ω and ζ are parameters characterizing the joint stiffness and damping, respectively.

Component-body modal data $[\boldsymbol{\alpha}_j^{(i)}, \boldsymbol{h}_j^{(i)}, \boldsymbol{K}^{(i)}]$ are needed to simulate dynamics using Eq. (13). A continuum representation of the mode shapes can be used for structural elements such as beams and plates. This also will enable the calculation of the momentum coefficients in a closed form.[5] However, complex structures such as solar arrays on GOES-8 necessitate a finite element approach for performing component-body eigenanalyses.

Obtaining the component-body data for use with the articulated, flexible multibody dynamics model is a two-step procedure for complex structures such as solar arrays. In the first step, a finite element component flexible body eigenanalysis is conducted to obtain the generalized mass and stiffness matrices and the associated mode shapes. When the modes of vibration are mass normalized, the modal mass matrix will be an identity matrix and the stiffness matrix will be diagonal with the squares of natural frequencies along the diagonal. The rigid body mass properties (mass, center of mass, and inertias) also are provided as a standard output from the same finite element analysis.

The calculation of the momentum coefficients $\boldsymbol{\alpha}_j^{(i)}$ and $\boldsymbol{h}_j^{(i)}$ for each mode constitutes the second step and can be achieved in a variety of ways. One way is to provide the finite element modal solutions as inputs to the flex-preprocessors for TREETOPS[2] and DISCOS.[3] A method for generating these coefficients directly inside a finite element solution sequence is given elsewhere.[7] A third way is to obtain these coefficients as the coupling terms in the Craig–Bampton mass matrix. The last approach is used in this study.

GOES-8 Component Mass and Stiffness Properties

The mass and stiffness properties for various GOES-8 components at the beginning of life are listed in Tables 1–3. The spacecraft body frame has a nadir pointing z axis, its y axis is opposite the orbit normal, and the x axis is obtained from the right-hand rule. The spacecraft body axes do not coincide with the principal axes. The solar array extends along the y direction. For the solar array and the solar sail, the reference point for the inertias are the interface points with the spacecraft bus.

The array consists of two solar panels connected via a hinge, and a small third panel as the outermost body. The innermost panel is connected to the $+y$ side of the spacecraft bus via a yoke. The cross section of the solar array consists of a 31.75-mm aluminum honeycomb core on both sides of which graphite face skins are bonded. In addition, the cell side consists of a kapton layer as well as the solar cells. A body frame is attached to the solar array at the interface between the solar-array yoke and the $+y$ end of the spacecraft bus, such that its y axis is along the length direction of the array and the body x axis is normal to the plane of the array.

Table 1 Component body mass properties

Component	Mass, kg	$\boldsymbol{r}_c^{(i)}$, m	$\boldsymbol{r}_i$, m	Inertia, kg·m^2		
Bus ($i = s$)	$m_s = 1035.6025$	0	0.01457	1028.8716	−10.9150	−23.6426
		0	−0.23450	−10.9150	1026.2444	−17.8563
		0	0.01566	−23.6426	−17.8563	1117.2465
Solar array	$m_1 = 85.7443$	−0.02045	−0.02764	1104.6067	9.3024	0.0576
($i = 1$)		2.91590	0.78871	9.3024	28.7784	2.2498
		−0.02455	−0.00844	0.0576	2.2498	1076.3055
Solar sail	$m_2 = 9.6788$	0	−0.11019	802.4238	0	0
($i = 2$)		−6.05443	−0.84560	0	0.24036	0
		0	−0.21164	0	0	802.4238

Table 2 Solar-array stiffness properties

	Mode 1 (OP1)	Mode 2 (IP1)	Mode 3 (OP2)	Mode 4 (T1)	Mode 5 (OP3)
$\boldsymbol{\alpha}^{(1)}$, $\sqrt{\text{kg}}$	6.362845	−0.000428	3.745014	−0.139602	3.858466
	−0.060110	0.061114	−0.346686	−0.007505	0.220996
	−0.000268	7.519367	0.001814	−0.196472	−0.000649
$\boldsymbol{h}^{(1)}$, $\sqrt{\text{kg}}\cdot\text{m}$	−0.001312	33.233892	0.002936	−0.326803	−0.006997
	−0.009509	0.329167	−0.067510	4.868742	−0.116229
	−31.935654	0.001202	−5.618361	0.128195	−3.833407
Diag$\sqrt{(\boldsymbol{K}^{(1)})}$, Hz	0.172617	0.692549	1.072639	1.832541	2.507761

Table 3 Solar-sail stiffness properties

	Mode 1 (B1)	Mode 2 (B2)	Mode 3 (T1)	Mode 4 (B3)	Mode 5 (B4)
$\boldsymbol{\alpha}^{(2)}$, $\sqrt{\text{kg}}$	0.375146	1.829846	0	−0.797597	0.643852
	0	0	0	0	0
	1.829846	−0.375146	0	−0.643852	−0.797597
$\boldsymbol{h}^{(2)}$, $\sqrt{\text{kg}}\cdot\text{m}$	−27.408293	5.619123	0	2.447389	3.031799
	0	0	0.490192	0	0
	5.619123	27.408293	0	−3.031799	2.447389
Diag$\sqrt{(\boldsymbol{K}^{(2)})}$, Hz	0.225012	0.225012	0.979085	1.796720	1.796720

Mass-normalized fixed-free component modes are obtained for the solar array via an eigenanalysis using NASTRAN. The fixed point is at the solar array–spacecraft interface. The parameters $\boldsymbol{\alpha}^{(1)}$, $\boldsymbol{h}^{(1)}$, and $\boldsymbol{K}^{(1)}$ for the solar array are listed in Table 2 for the first five vibrational modes. The fixed-free modes have the property that each of these modes may have nonzero linear and angular momentum coefficient components[5,6] associated with each axis of the body frame. These coefficients provide a measure of how much the vibration of the solar array contributes to the linear and angular momenta of the spacecraft, with the spacecraft and component-body frames chosen as above. The momenta will not be conserved without these contributions even in the case of no external excitations.

Based on the physical characteristics of the array, the array modes can be characterized as in-plane (IP) bending, out-of-plane (OP) bending, or torsion (T). Referring to Table 2, we observe that the OPj ($j = 1, 2, 3$) modes have the largest value in the first row of $\boldsymbol{\alpha}^{(1)}$, the array x direction. This implies that the array bends along the body x axis in these modes of vibration. Note that a large displacement along the x axis also implies a large rotation about the z axis, and vice versa. Consequently, we observe that the OPj modes contribute largest to the third row of $\boldsymbol{h}^{(1)}$. Similarly, IP1 has the largest entry in the (3,2) element of $\boldsymbol{\alpha}^{(1)}$ and thus would correspond to the displacement of the array along the z axis, i.e., in the y-z plane. Therefore, the corresponding largest angular momentum coefficient can be found as $\boldsymbol{h}^{(1)}(1, 2)$. Finally, for the only torsional mode that is present in the first five modes, the largest component in $\boldsymbol{h}^{(1)}$ is about the y axis, as to be expected. This mode also has significantly smaller linear momentum contribution than the bending modes. Note that all of the modes have the x, y, and z spatial dependency, as can be seen from the populated $\boldsymbol{\alpha}^{(1)}$ and $\boldsymbol{h}^{(1)}$ matrices. Although the modes have been characterized as IP, OP, and T, none of the modes is purely IP, OP, or T, as can be seen from Table 2.

The solar sail is a long flexible truss structure that is rigidly attached to the $-y$ side of the spacecraft and extends along the spacecraft negative y axis. Fixed-free component modes are used for the sail as well. The associated component natural frequencies and the momentum coefficients $\boldsymbol{\alpha}^{(2)}$ and $\boldsymbol{h}^{(2)}$ are listed in Table 3. For this boom-like structure, the modes can only be characterized as bending (B) and T. Although there are repeated frequencies, they correspond to bending in each of the y-z and the x-z planes, implying that the eigenvectors for repeated frequencies are linearly independent.

Component vs System Frequencies

In structural dynamics, where no large articulation is permitted, the development of component-mode synthesis[4] was necessitated by the enormous task of modeling large aircraft as single bodies. The system frequencies are obtained from a synthesized structural model assembled from reduced-order component models. When articulation is present, however, component flexible-body models must be used in conjunction with articulated, flexible multibody dynamics approaches.[1–3] In this case, the system frequencies are not known until the eigenvalue problem for a linearized dynamic model of the entire system is solved. The $\boldsymbol{\alpha}^{(1)}$ and $\boldsymbol{h}^{(1)}$ properties of the selected component-mode set have a significant effect on these frequencies. This also raises the issue of what component modes must be used and how the component frequencies are affected when the whole system is synthesized.

Using a uniform articulated flexible beam as an example, it has been shown[5] that when the component-mode set represents a body that is more constrained than the component in the physical system, the system frequencies obtained from the linearized articulated multibody model will be higher than the respective component frequencies. Fixed-free modes were used to represent a pinned-free flexible beam undergoing articulation, and the system frequencies were closer to but higher than the pinned-free frequencies. Table 4 demonstrates this fact for GOES-8 and also that it is these system frequencies that must be expected in the flight data. At the system level the array and the sail have a different end condition (large, moving end mass and inertia of the spacecraft bus) from the fixed-end condition that was employed at the respective interfaces with the spacecraft bus during component-body modeling.

Table 4 Component and system frequencies

Component	Component frequencies, Hz	System frequencies, Hz: Present method	System frequencies, Hz: One-body NASTRAN analysis
Solar array	0.17262	0.19950	0.19960
	0.69255	1.14354	1.12163
	1.07264	1.11905	1.11077
	1.83254	1.85410	1.85243
	2.50776	2.59547	2.57851
	2.81275	2.90904	2.91283
	3.26070	3.26193	3.26067
Solar sail	0.22501	0.25791	0.25682
	0.22501	0.33056	0.33677
	0.97909	0.97920	0.97882
	1.79672	1.81379	1.81375
	1.79672	1.82298	1.81908

The initial orientation angle is set to $\theta = 0$ deg, the solar array is assumed to be locked, the system of equations in Eq. (13) is linearized, and the associated eigenvalue problem is solved to obtain the system frequencies. Table 4 shows these results for $N_1 = 7$ and $N_2 = 5$. Only the nonzero frequencies are shown here. The first column in Table 4 describes the component, the second column contains the component frequencies, and the third column contains the corresponding frequencies obtained by solving the eigenvalue problem mentioned above. Note that each system frequency is higher than the associated component frequency because of the differences in the end conditions described in the preceding paragraph. The change in the boundary condition has the most significant effect on the solar-array IP1 mode. It is shown in the "Comparison of Flight Data and Simulation Results" section that this observation is crucial to understanding the flight data.

The system frequencies obtained via a one-body finite element analysis for the whole system, with a rigid bus, are shown in the last column in Table 4. The results are very close, thus providing confidence in both the articulated multibody dynamic modeling approach and the appropriate use of model data. Modal truncation accounts for some of these differences. In general, it is rarely feasible to set up one-body models and verify the system frequencies this way for large systems. Finally, note that the same sail component frequencies give rise to quite different system frequencies. This is because the spacecraft inertias are different in different directions, and a lower inertia in one direction results in a higher frequency for vibration corresponding to that direction.

Flight Data

The flight data for day 103 (April 13) of 1995 is used for comparison. These data were obtained for a short period around the top of each hour for 23 consecutive hours. The sampled data are at 800 Hz (Nyquist frequency, 400 Hz) and, consequently, only data corresponding to slightly over 5 min and 27 s (2^{18} samples) are collected in each data set to provide a resolution of 0.003 Hz ($=400/2^{17}$) in the frequency spectrum. The ADS is a high-pass filter with a 2-Hz cutoff. Hence, the flight data are corrected for the low-frequency attenuation by using the inverse of the known ADS transfer function. A 10-s strip of the time-domain data representing a steady state, after the filter transients are attenuated, then is considered for comparison. Because all of the disturbances on the spacecraft are not modeled, this may correspond to different time periods in each data set. For example, the 10-s strip may correspond to the 170- to 180-s portion of the data for one case, and the 30- to 40-s portion of the data for another case, and so on.

Power spectral density (PSD) plots were generated with the 2^{18} length corrected samples. The ADS outputs are typically in the $[-20, 20]$ μ rad range and, at this level, the spacecraft responses are very sensitive to the smallest disturbance. All such disturbances are not modeled. After discounting the known instrument disturbances, it was found that the PSD peaks corresponded to 0.5917, 1.1834, and 1.7751 Hz. Note that 0.5917 Hz ($=1/1.69$) is the frequency of the stepping of the solar array and 1.1834 Hz and 1.7754 Hz are its second and third harmonics, respectively. In general, the peaks at

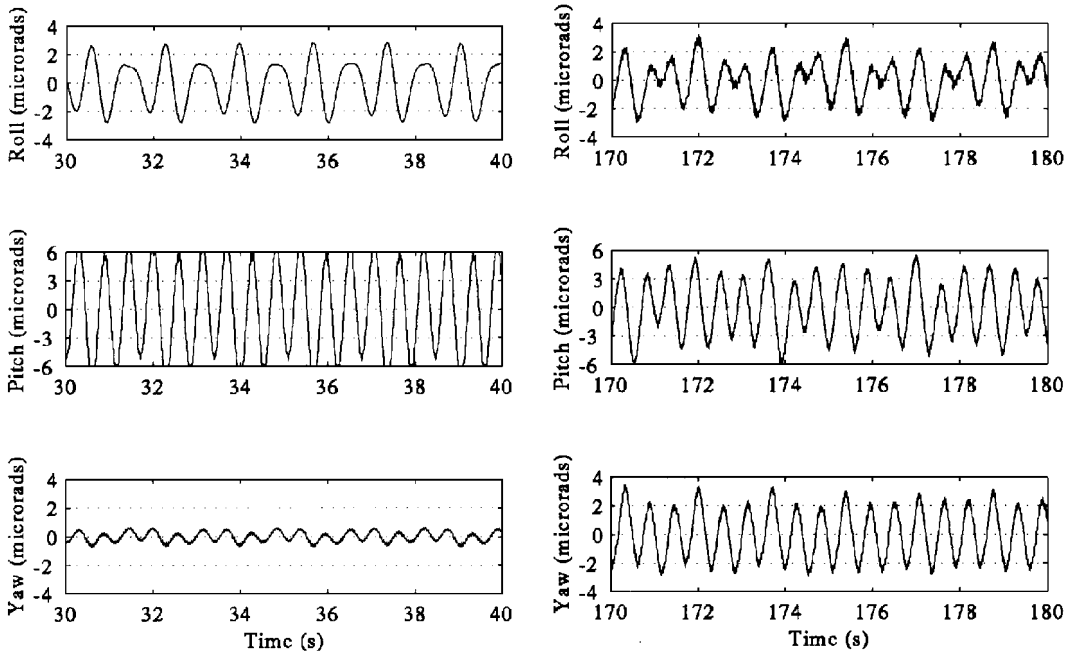

Fig. 3 Flight data around 11:00:00 GMT and simulated time history with nominal parameters for $\theta = 0$ deg.

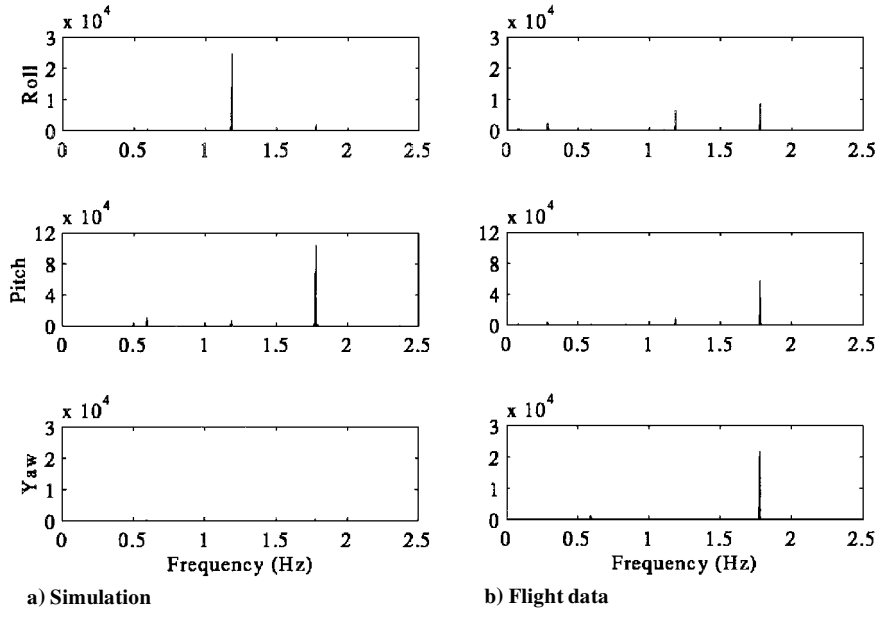

Fig. 4 PSD plots for the time histories in Fig. 3.

0.5917 Hz are much smaller than those at the other two frequencies. Referring to Table 4, we observe that this is because these harmonics are close to the system frequencies that arise from the IP1 (and with enough parametric uncertainties, to OP2) and T1 frequencies of the solar array. Note that by considering only component modal frequencies one may conclude incorrectly that the second harmonic is closest to the OP2 modal frequency. The excitation may not be characterized as resonance, but these harmonics clearly lie close to the *system* natural frequencies.

Comparison of Flight Data and Simulation Results

The attitude control for the spacecraft is via independent pitch and roll/yaw controllers. The bandwidth for the pitch controller is 0.05 rad/s and that for the roll/yaw controller is in the range 0.005–0.0125 rad/s. Because all structural frequencies are well outside the bandwidth of the attitude controllers, no attitude control is considered. Only the (internal) stepping action is considered as the excitation in the system. Simulation results are obtained by numerically integrating the dynamic equations in Eq. (13), with $N_1 = 5$ and $N_2 = 2$. The spacecraft rigid-body response is removed from the simulated attitude response by using a high-pass digital filter with a very low cutoff frequency.

Figure 3 compares the simulated results for $\theta(t = 0) = 0$ deg case with the nominal spacecraft data listed in Tables 1–3, and the flight data around 11:00:00 Greenwich Mean Time (GMT). The effect of stepping can be seen clearly in these plots. Although the roll magnitudes compare reasonably well, the roll shape as well as pitch and yaw amplitudes are quite different. We find the reason in Fig. 4 where the PSDs for the roll, pitch, and yaw (RPY) for the above simulated results and the PSDs for the flight data are plotted. Note the small peak at the 1.7751-Hz frequency in roll and the almost absence of the same in yaw, in the simulated results. The PSD plots for all of the other 22 sets of the flight data also showed similar behavior. Although this frequency does not coincide with the known T1 modal frequency of the solar array, it is closest only to this system mode, and the stepping action is expected to excite the torsional mode.

Similarly, we conclude that the 1.1834-Hz frequency in the flight roll PSD is close enough to the array IP1 mode to excite it.

The PSD plots in Fig. 4 imply that the T1 mode is not sufficiently coupled, and the IP1 mode may be coupled too much, with the roll for $\theta(t = 0) = 0$-deg case, in the dynamic model. Since the coupling of a mode to attitude motion is through the rigid-elastic coupling terms (linear and angular momentum coefficients), we conclude that the nominal values for these coefficients for the IP1 and the T1 modes given in Table 2 do not adequately represent the solar-array on-orbit vibrational behavior.

Parametric studies were then conducted to determine the appropriate values for the array momentum coefficients for the IP1 and T1 modes in order to obtain a good agreement between the flight data and the simulation results. Referring to the mass matrix in Eq. (3) and the solar-array modal momentum coefficients in Table 2, we observe that the elements in the second row of the term $\tilde{\boldsymbol{r}}_1 \boldsymbol{C}_1^s \boldsymbol{\alpha}^{(1)} + \boldsymbol{C}_1^s \boldsymbol{h}^{(1)}$ determine how much the spacecraft pitch is affected directly due to the solar-array stepping, and the remaining rows determine how much roll and yaw are affected indirectly through the coupling with the pitch. For the properties given in Tables 1 and 2, it turns out that $\boldsymbol{h}^{(1)}$ contributes most to this term. Since the simulated pitch in Fig. 3 is much larger than the flight pitch, we conclude that the magnitude of the element $\boldsymbol{h}^{(1)}(2, 4)$ must be reduced. In addition, $\boldsymbol{\alpha}^{(1)}(1, 4)$ and $\boldsymbol{\alpha}^{(1)}(3, 4)$ also needed to be modified. Similarly, because the array T1 mode is almost absent from the simulated roll and yaw, we conclude that the magnitudes of (1, 4) and (3, 4) elements of $\boldsymbol{h}^{(1)}$ must be increased. A question on the sign of these elements remained. Simulation results showed that $\boldsymbol{h}^{(1)}(1, 4)$ must be negative and $\boldsymbol{h}^{(1)}(3, 4)$ must be positive. Negative values for $\boldsymbol{h}^{(1)}(3, 4)$ resulted in numerical instabilities. The component frequency for the T1 mode also was considered as a parameter because the excitation of the T1 mode depends on how close this frequency is to the third harmonic of solar-array stepping.

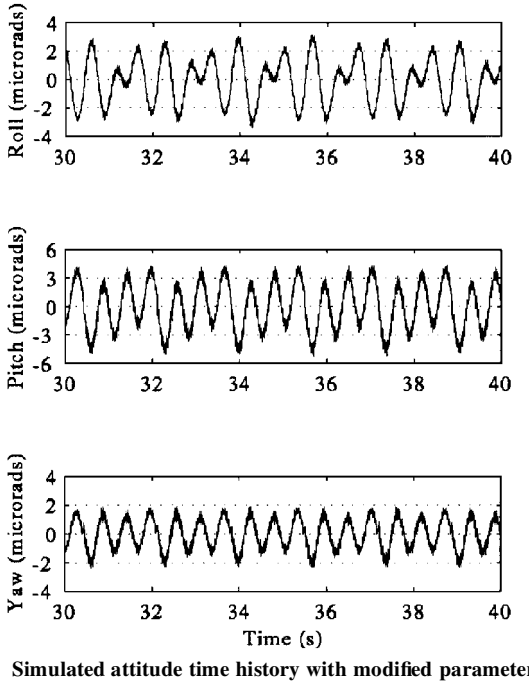

Fig. 5 Simulated attitude time history with modified parameters for $\theta = 0$ deg.

The IP1 peak in simulated roll in Fig. 4 is about three times that of the flight roll, and this implies that the nominal value of $\boldsymbol{h}^{(1)}(1, 2)$, for the IP1 mode, used in the simulation is too large. It was found that this value must be reduced and the $\boldsymbol{h}^{(1)}(2, 2)$ and the $\boldsymbol{h}^{(1)}(3, 2)$ must be slightly increased to match the flight data. A discussion on what these parameter modifications imply is presented in the Discussion section.

The discussion in the preceding two paragraphs only points to how these coefficients must change but does not tell by how much. Linear eigenanalyses and Bode plots of the transfer functions also did not help. Good matches with flight data were obtained only after time-consuming numerical simulations. The parameters that resulted in successful matches are shown in Table 5 for various configurations of the solar array.

Last but not least is the question of what value must be used for Ω in Eq. (14). The test data indicated too stiff a value to be useful in these simulations. The roll for the $\theta = 0$ deg case and the yaw for the $\theta = -90$ deg case were found to be sensitive to this stiffness. For the results presented here, $\Omega = 80$ rad/s and $\zeta = 0.1$. The parametric studies indicated that larger and smaller values for the joint stiffness result in larger and smaller high-frequency oscillations, respectively. However, smaller Ω values result in larger amplitude low-frequency (IP1 and T1) oscillations, and vice versa.

Figure 5 shows the simulated RPY time history for $\theta(t = 0) = 0$ deg and with the modified coupling terms shown in Table 5. In all cases, initial data that contained dynamic/filter transients have been discarded. Simulation results in Fig. 5 are in good agreement with the flight data shown in Fig. 3b. Figure 6 shows similar comparison for

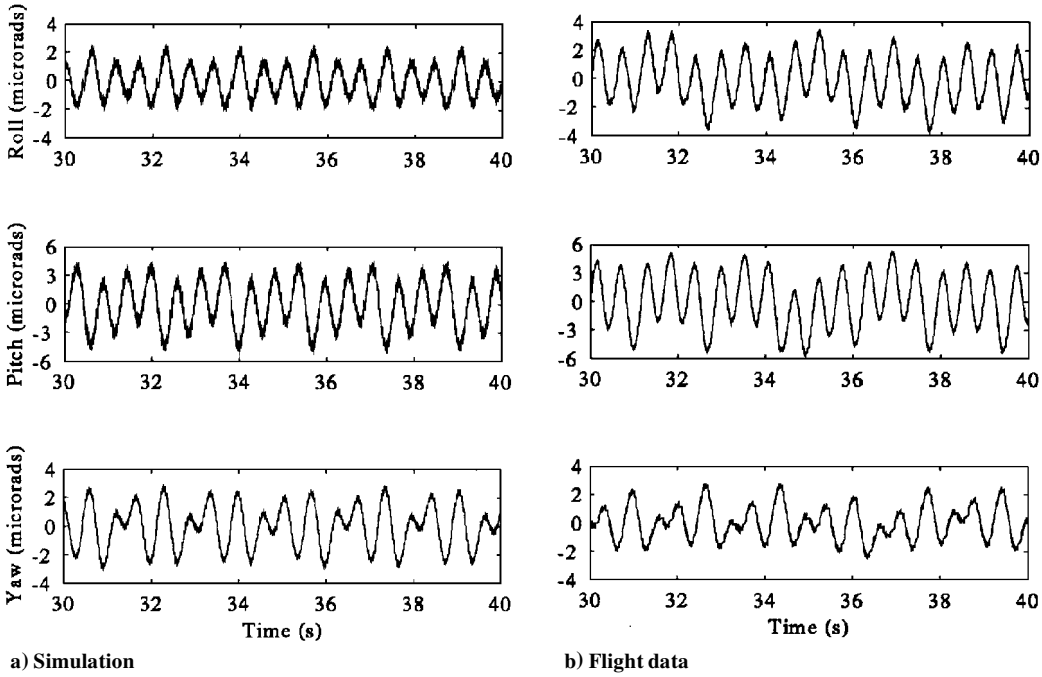

a) Simulation **b) Flight data**

Fig. 6 Flight data around 05:00:00 GMT and simulated time history with modified parameters for $\theta = -90$ deg.

Table 5 Parameter modifications needed for matching flight data

Solar-array orientation	Spacecraft attitude DOF	Linear momentum coefficients $\alpha^{(1)}$, $\sqrt{\text{kg}}$		Angular momentum coefficients $h^{(1)}$ $\sqrt{\text{kg}} \cdot \text{m}$		Component T1 modal frequency, Hz
		IP1	T1	IP1	T1	
$\theta = -90$ deg	Roll (x)	−0.0004	−0.3970	30.2520	−1.8487	
and 0 deg	Pitch (y)	0.0611	−0.0079	0.6723	4.3697	1.8325
	Yaw (z)	7.5194	−0.3308	1.3916	1.6807	
$\theta = 45$ deg	Roll (x)	−0.0004	−0.2647	26.8907	−1.8487	
	Pitch (y)	0.0609	−0.0079	0.6723	4.3697	1.79
	Yaw (z)	5.2934	−1.0587	−1.3916	−0.8403	
$\theta = 90$ deg	Roll (x)	−0.0004	−0.7940	26.8907	−1.1765	
	Pitch (y)	0.0609	−0.0079	0.6723	4.3697	1.79
	Yaw (z)	6.6168	−0.2647	−1.3916	1.6807	

the simulation results with $\theta(t = 0) = -90$ deg and the flight data around 05:00:00 GMT. The high-frequency oscillations in Figs. 5 and 6 are due to the stepper motor stiffness.

Table 5 lists the values for the momentum coefficients that are needed for a good comparison with the flight data for various times of the day. These variations can be explained as follows. Since the spacecraft moves from a midnight to a noon configuration and then back over a 24-hour period, the sun is expected to have significant time-varying effects on the shape and hence on the vibrational behavior of the array. This was indeed found to be the case because these coefficients had to be adjusted for each value of θ.

Discussion

Recall that we mentioned earlier that the momentum coefficients are associated with modes of vibration and that they are calculated after the modal solution is obtained. The disagreement between the flight data and the simulation results with the nominal parameters implies that the on-orbit array behaves differently, and may be physically different, from the modeled array. If the physical array is available, the two-step procedure outlined in the Dynamic Model section must be followed for obtaining a better model. In the case of the on-orbit array, because the physical structure was not available for modeling, the first step mentioned above was eliminated from the parametric study and the parameters listed in Table 5 were selected only on the basis of matching the flight response. This has the drawback of not knowing how each point on the solar array vibrates because the modal vectors are not available and momentum coefficients present only condensed information. However, this information is not required for comparison with the ADS data because the ADSs are mounted on the spacecraft bus. Since the yoke is very close to the south end of the bus, it can be assumed that the modal vectors at the SXI mounting locations remain unchanged for predicting the SXI jitter.

From a comparison of the solar-array nominal vibrational characteristics (Table 2) and the modified characteristics (Table 5), we note how different the behaviors of the on-orbit solar array and the nominal array are. Significant $\boldsymbol{h}^{(1)}(1, 4)$ and $\boldsymbol{h}^{(1)}(3, 4)$ components for the T1 mode imply that as the solar array twists, it also bends considerably. For the IP1 mode, a significant value for $\boldsymbol{h}^{(1)}(2, 2)$ indicates that the array in-plane motion also results in torsional motion. The reduced value for $\boldsymbol{h}^{(1)}(1, 2)$ in Table 5 implies that this mode now contributes less to the x component (in body frame) of the angular momentum than the IP1 mode of the nominal array.

What are the reasons for this discrepancy? The reasons are essentially the assumptions made while building the model—both at the component level and at the multibody model level. First, the component level assumptions: 1) Equivalent membrane and bending stiffnesses were used for the development of component-body models for a multilayered solar array, 2) chemical bonding between the layers of the solar array was not modeled in the finite element model, and 3) thermal loads or thermal structural interactions were not modeled. Consequently, the effect of bonding on the vibrational modes, and the effect of differential heating across the array cross section, especially with the chemical bonding adequately modeled, were not addressed. This can be significant considering that a separate thermal analysis[8] of the array showed that the array bends away from the sun with a tip deflection of about 6.25 cm, and this can account for the coupling between the torsional and bending motions. Note that a component-level thermal model for the array was built and analyzed prior to the commission of this study.

At the multibody-model level, the assumption involves neglecting thermal loads. These loads may be treated as those giving rise to prestressed conditions. Differential stiffness matrices[9] can be employed for modeling these time-varying loads and can be added to the model described in the Dynamic Model section. However, it was not pursued here because of the complexity and the fact that the array component model was developed elsewhere. At present, none of the software codes (TREETOPS,[2] DISCOS,[3] etc.) available for modeling articulated, flexible multibody systems have the capability to consider thermal–structural interactions.

Finally, some details on the numerical integration aspects of this study are in order. It was demonstrated that the flight data and simulation results can be shown to have good agreement at subarcsecond levels, even with the limitations mentioned above. Such a precision, however, requires that numerical integration be performed with a tight tolerance—of at least 10^{-7} on the states. Further complicating the simulation is the fact that the system in Eq. (13), combined with Eq. (14) and the joint stiffness considered in this study, is a stiff system. These two factors result in very slow simulation speeds. Increasing the stepper motor stiffness slows down the simulation even further. In addition, because the simulations start with modal rates and modal amplitudes that are bound to be different from the steady-state results shown in Figs. 5 and 8, it is imperative that the simulations be conducted long enough to attenuate the transients. The simulations were conducted in a MATLAB®/SIMULINK environment on a Sun Sparc 20 workstation.

Conclusions

The attitude dynamics of GOES-8 is simulated using an articulated, flexible multibody approach and simulation results are compared with the spacecraft flight data. The solar array and the solar sail are the primary flexible bodies on the spacecraft, and the solar array is articulated by a stepper motor.

Simulation results obtained using the nominal modal solar-array data were not in agreement with the flight data. After time-consuming parametric studies resulted in the successful matching of the flight data, it was concluded that the vibrational characteristics of the solar array during day 103 of 1995 were substantially different from the nominal/design values. The parameter modifications required in order for the simulation results to agree with the flight data were different for different times of the day, and were attributed to the effects of the sun and the assumptions behind the current model.

This study shows that multibody dynamics approaches can be employed to model the dynamics of any spacecraft although GOES-8 spacecraft was not set up to provide a platform for validating multibody dynamics approaches. However, the modeling of GOES-8 using an articulated, flexible multibody approach provided valuable insight into the issues associated with modeling three-dimensional systems consisting of non-beam-like flexible bodies operating in a real-world environment. This study points out that the effects of modeling assumptions made both at the component and multibody levels and the limitations of such models must be understood. For

example, although several articulated, flexible multibody dynamics software packages are available, none of them model thermal–structural interactions. To the best of the author's knowledge, none of these packages have been employed to simulate real-world spacecraft data to the accuracies considered here.

Acknowledgments

This work was performed under contract to NASA Goddard Space Flight Center (GSFC), Contract NAS5-32590. The author gratefully acknowledges the support of Sandra Cauffman, Instrument Manager, GOES project. Thanks are also due to Mike Hagopian of NASA GSFC for his valuable comments and Wayne Dellinger of Swales & Associates, Inc., for providing the GOES-8 flight data, and Sharad Mehta of Space Systems/Loral for providing the component modal data from NASTRAN analyses.

References

[1]Hooker, W. W., "Equations of Motion for Interconnected Rigid and Elastic Bodies: A Derivation Independent of Angular Momentum," *Celestial Mechanics*, Vol. 11, 1975, pp. 337-359.

[2]Singh, R. P., VanderVoort, R. J., and Likins, P. W., "Dynamics of Flexible Bodies in Tree Topology—A Computer-Oriented Approach," *Journal of Guidance, Control, and Dynamics*, Vol. 8, No. 5, 1985, pp. 584–590.

[3]Bodley, C., Devers, A., Park, A., and Frisch, H., "A Digital Computer Program for Dynamic Interaction and Simulation of Controls and Structures (DISCOS)," NASA TP 1219, 1978.

[4]Meirovitch, L., *Computational Methods in Structural Dynamics*, Sijthoff and Noordhoff, Alphen aan den Rijn, The Netherlands, 1980.

[5]Tadikonda, S. S. K., Mordfin, T. G., and Hu, T. G., "Assumed Modes Method and Articulated Flexible Multibody Dynamics," *Journal of Guidance, Control, and Dynamics*, Vol. 18, No. 3, 1995, pp. 404–410.

[6]Hughes, P. C., "Modal Identities for Elastic Bodies, with Application to Vehicle Dynamics and Control," *Journal of Applied Mechanics*, Vol. 47, March 1980, pp. 177–184.

[7]Messac, A., and Storch, J., "Evaluation of Inertial Integrals for Multibody Dynamics," *Journal of Guidance, Control, and Dynamics*, Vol. 17, No. 3, 1994, pp. 624–626.

[8]Anon., "GOES IJK/LM Solar Array Package, Vol. 2," Space Systems/Loral, Document No. WDL-TR11190, Palo Alto, CA, Dec. 1987, Sec. 3.2.

[9]Cook, R. D., *Concepts and Applications of Finite Element Analysis*, McGraw–Hill, New York, 1985.